Journal of Biomedical Optics 9(4), 753–759 (July/August 2004)

Interaction of PSD-95 with potassium channels visualized by fluorescence lifetime-based resonance energy transfer imaging

Christoph Biskup
Laimonas Kelbauskas
Thomas Zimmer
Klaus Benndorf
Friedrich-Schiller-Universität Jena
Institut für Physiologie II
Teichgraben 8
07740 Jena
Germany
Phone: ++49-3641-938874
Fax: ++49-3641-933202
E-mail: christoph.biskup@mti.uni-jena.de

Axel Bergmann
Wolfgang Becker
Becker & Hickl GmbH
Nahmitzer Damm 30
12277 Berlin
Germany

J. Peter Ruppersberg
SEED GmbH
Wöhrdstr. 5
72072 Tübingen
Germany

Clemens Stockklausner
Nikolaj Klöcker
Albert-Ludwigs-Universität Freiburg
Dept. of Physiology II
79104 Freiburg
Germany

Abstract. Resonance energy transfer (RET) has been extensively used to estimate the distance between two different fluorophores. This study demonstrates how protein–protein interactions can be visualized and quantified in living cells by time-correlated single-photon counting (TCSPC) imaging techniques that exploit the RET between appropriate fluorescent labels. We used this method to investigate the association of the potassium inward rectifier channel Kir2.1 and the neuronal PDZ protein PSD-95, which has been implicated in subcellular targeting and clustering of ion channels. Our data show that the two proteins not only colocalize within clusters but also interact with each other. Moreover, the data allow a spatially resolved quantification of this protein–protein interaction with respect to the relative number and the proximity between interacting molecules. Depending on the subcellular localization, a fraction of 20 to 60% of PSD-95 molecules interacted with Kir2.1 channels, approximating their fluorescent labels by less than 5 nm. [DOI: 10.1117/1.1755721]

Keywords: resonance energy transfer, fluorescence lifetime imaging (FLIM), postsynaptic density protein (PSD-95), inwardly rectifying potassium channels

Paper 03091 received Jul. 8, 2003; revised manuscript received Sep. 29, 2003; accepted for publication Oct. 23, 2003.

1 Introduction

Membrane-associated guanylate kinases (MAGUKs) organize macromolecular protein complexes at specialized membrane domains.[1–4] In addition to providing a scaffold by offering multiple domains for protein–protein interactions, they can also function in subcellular targeting of their binding partners. Neuronal MAGUKs of the postsynaptic density-95 (PSD-95) family have thus been implicated in synaptic development and plasticity.[5–7] To date, most studies on MAGUK protein–protein interactions have used biochemical binding assays that provide only a static insight, a ''snapshot,'' of the cellular events; i.e., biochemical binding assays do not allow one to follow protein–protein interactions in living cells. Improved understanding of MAGUK actions, however, will require visualization of protein–protein interactions in living cells with both spatial and temporal resolution.

Fluorescence microscopy employing fluorescent proteins is ideally suited for studying the subcellular localization of proteins in living cells. Moreover, the photophysical properties of a fluorophore can be exploited to obtain additional information on its immediate molecular environment. Relaxation of a fluorophore from its excited state to the ground state can be accelerated by various processes. In the presence of an appropriate acceptor, the relaxation from the excited state can be accelerated by a physical process termed resonance energy transfer (RET).

For RET to occur, the emission spectrum of a donor fluorophore needs to overlap with the absorption spectrum of the acceptor fluorophore. In addition, both fluorophores have to be in very close spatial proximity since the efficiency of RET depends on the inverse sixth power of the distance between donor and acceptor.[8–10] RET efficiency can thus provide information on inter- or intramolecular distances in the range of a few nanometers.[11,12] When RET occurs, both the intensity and lifetime of the donor fluorescence decrease, while the intensity of the acceptor emission increases. This offers two different approaches for determining RET efficiency: one detects changes in the intensity of donor and acceptor emissions, the other one measures changes in the fluorescence lifetime of the donor molecule. For technical reasons, most methods estimate RET efficiency from changes in the intensity of donor

Address all correspondence to Dr. Christoph Biskup, Klinikum der Friedrich-Schiller-Universität Jena, Institut fuer Physiologie II, Teichgraben 8, D 07740 Jena, Germany. Tel: 49-3641-938874; Fax: 49-3641-933202; E-mail: christoph.biskup@mti.uni-jena.de

1083-3668/2004/$15.00 © 2004 SPIE

and acceptor emission. They bear the disadvantage, however, that one needs to correct for crosstalk between donor and acceptor emission channels and to correlate donor and acceptor concentrations.[13,14] In contrast, determining RET efficiency by changes in the donor lifetime can dispense with such mathematical corrections, if measurements of the donor fluorescence decay are restricted to the part of the donor emission spectrum that is devoid of acceptor fluorescence.

In this study, we demonstrate how the time-correlated single-photon counting (TCPSC) technique can be used in conjunction with a laser scanning microscope and a pulsed excitation source to record donor fluorescence lifetimes as a reliable measure of RET efficiency between interacting proteins. The technique is based on a three-dimensional histogramming process that records photon density over the time and the spatial coordinates of the scanning area. The histogramming process avoids any time gating or wavelength scanning and hence can yield a near-perfect counting efficiency. We employed this technique to characterize and quantify the interaction between the neuronal MAGUK protein PSD-95 and the inward rectifier potassium channel Kir2.1 in living cells.

2 Materials and Methods

2.1 *Recombinant DNA Procedures*

N-terminal fusion constructs of Kir2.1 with enhanced green fluorescent protein (EGFP) or its spectral variants enhanced cyan and yellow fluorescent protein (ECFP, EYFP), were designed by inserting mKir2.1 cDNA in-frame into the respective ExFP-C1 eukaryotic expression plasmid (Clontech Laboratories). Likewise, C-terminal fusion constructs of PSD-95 with fluorescent proteins were designed by inserting the rPSD-95 cDNA into the respective ExFP-N1 expression plasmid. Channel mutants were constructed by polymerase chain reaction (PCR) with oligonucleotides carrying the desired mutations. For the YFP–CFP hybrid protein, EYFP and ECFP sequences were fused by recombinant PCR and subcloned into the mammalian expression vector pcDNA3 (Invitrogen) to yield expression of the following protein: $EYFP_{(1\text{-}239)}$-GSGSGSGDEVDGGSGSGV-$ECFP_{(1\text{-}239)}$. All PCR-derived constructs were verified by sequencing.

2.2 *Cell Culture and Transfection*

Human embryonic kidney 293 (HEK293) and opossum kidney (OK) cells (American Type Culture Collection) were grown in Dulbecco's modified Eagle's medium (DMEM) and DMEM-F12 (Invitrogen), respectively, supplemented with 10% fetal calf serum and 1% penicillin/streptomycin (Invitrogen) at 37 °C and 5% CO_2. At ~80% confluence, the cells were transfected with the respective cDNAs using a conventional calcium phosphate precipitation technique for HEK293 and Effectene reagent (Qiagen) for OK cells. For confocal imaging and lifetime measurements, the coverslips were transferred to a microscope chamber superfused with buffered saline solution containing (in mmol l^{-1}): Na 145, K 5, ethylene glycol-bis(2-aminoethylether)-*N*,*N*,*N*′,*N*′-tetraacetic acid (EGTA) 1,*N*-(2-hydroxyethyl)piperazine-*N*′-(2-ethanesulfonic acid) (HEPES) 5, pH 7.4.

2.3 *Coimmunoprecipitation and Western Blot Analysis*

Two days after transfection, HEK293 cells were lysed in TEEN-T (50 mM Tris pH 7.6, 1 mM EDTA, 1 mM EGTA, 150 mM NaCl, 1% Triton X-100, Complete protease inhibitor cocktail, Roche) for 30 min on ice. Nuclei and cell debris were pelleted by low-speed centrifugation at 500 *g* for 5 min at 4 °C. Green fluorescent protein (GFP)-fused Kir2.1 was precipitated with a monoclonal mouse anti-GFP antiserum (Molecular Probes), followed by incubation with Protein A sepharose beads (Pharmacia) to capture the antibody protein complexes. After washing with TEEN-T, the precipitates were separated by reducing sodium dodecylsulfate-polyacrylamide gel electrophoresis (SDS-PAGE) on a 10% polyacrylamide gel, transferred onto PVDF membranes and incubated with a mouse monoclonal anti-GFP antibody (1:5000; Clontech Laboratories) and a monoclonal anti-PSD-95 antibody (1:2000; Affinity BioReagents). Following incubation with horse radish peroxidase (HRP)-conjugated anti-mouse immunoglobulin G (IgG) (1:2500; Santa Cruz Biotechnologies), labeled proteins were detected using ECL-plus reagent (Amersham).

2.4 *Confocal Laser Scanning Microscopy*

Confocal imaging was performed with a Zeiss laser scanning microscope (LSM 510, Carl Zeiss, Göttingen, Germany) using a Zeiss C-Apochromat 63× (NA 1.20) water immersion objective. Cyan fluorescent protein (CFP) and yellow fluorescent protein (YFP) were excited with the 458- and 514-nm lines of an Ar^+ laser, respectively. Fluorescence was recorded with a 470 to 500-nm bandpass (CFP) and a 530-nm longpass filter (YFP).

3 Results and Discussion

3.1 *PSD-95 Interacts with Kir2.1 in a PDZ-Mediated Fashion*

Upon heterologous expression in epithelial cells, GFP-fused wild type Kir2.1 (GFP-Kir2.1) was homogeneously distributed within the plasma membrane and the Golgi complex [Fig. 1(A) a].[15] Coexpression of PSD-95 directed the channel into clusters in which both proteins colocalized [Fig. 1(A) b,c]. Cluster formation was prevented when PSD-95 was coexpressed with Kir2.1 lacking the last three C-terminal amino acids -*S*-*E*-*I* (GFP–Kir2.1–Δ426–428), which match the consensus binding sequence -*S*/*T*-*X*-*I*/*V*/*L* specifically recognized by class I PDZ domains.[16,17] Biochemical experiments confirmed these findings as PSD-95 coimmunoprecipitated with GFP–Kir2.1, but not with GFP–Kir2.1–Δ426–428 [Fig. 1(B)]. These results are in good agreement with experiments by Nehring and co-workers showing coprecipitation of myc-tagged Kir2.1 and PSD-95.[18] A schematic drawing illustrating the PDZ-mediated interaction between Kir2.1 and PSD-95 is shown in Fig. 1(C).

3.2 *Experimental Setup for Spatially Resolved Fluorescence Lifetime Measurements*

Coimmunoprecipitation experiments neither allow one to study protein–protein interactions within specific subcellular domains nor can they trace the time course of protein–protein

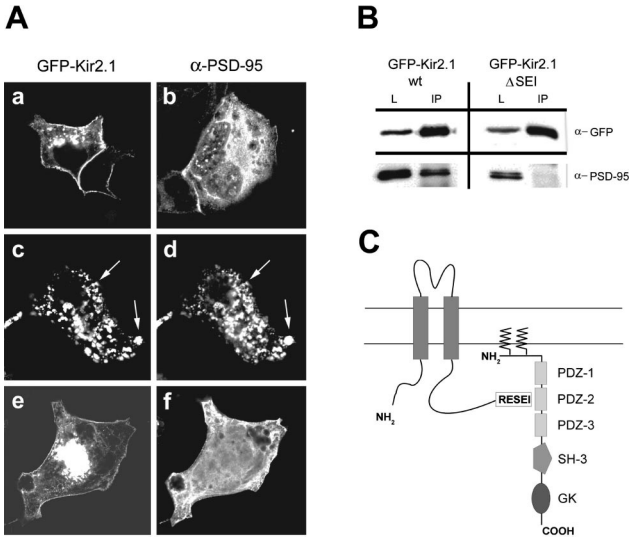

Fig. 1 PSD-95 clusters the potassium inward rectifier Kir2.1 in a PDZ-mediated fashion. (A) Representative images of OK cells expressing (a) either GFP–Kir2.1 (b) PSD-95 alone or (c) and (d) coexpressing both proteins. Fluorescence images recorded in the GFP channel are displayed on the left side (a), (c), (e). PSD-95 expression was detected by immunocytochemistry and visualized by a Cy3-conjugated secondary antiserum (b), (d), (f). Note that coexpression induces cluster formation in which both proteins colocalize [arrows in (c) and (d)]. Deletion of the PDZ ligand domain of Kir2.1 (Kir2.1–ΔSEI) prevents cluster formation (e) and (f). (B) PSD-95 coimmunoprecipitates with wild type (wt) GFP–Kir2.1 but not with GFP–Kir2.1–ΔSEI. L; load (10% of total input); IP; immunoprecipitate. (C) Schematic drawing of the Kir2.1–PSD-95 protein–protein interaction. PSD-95 comprises three N-terminal PDZ domains, an SH3, and a C-terminal GK domain, which all serve as protein interaction modules. PDZ-1 and PDZ-2 are class I PDZ domains that preferentially bind to the consensus sequence of *-S/T-X-I/V/L* harbored by the Kir2.1 channel C-terminus. The tandem arrangement of PDZ-1 and PDZ-2 has been proposed to favor interactions with multimeric membrane proteins such as ion channels and receptors,[17] but the exact stoichiometry of PSD-95 interactions is still unknown. PSD-95 is associated with cellular membranes via palmitoylation of two N-terminal cysteine residues.

interactions in single living cells. Conclusions about the nature of such interactions can only be drawn from large populations of cells. A fluorescence lifetime imaging approach that permits visualization of the extent of RET between interacting proteins can overcome these limitations.

PSD-95 and Kir2.1 were labeled with the cyan- and yellow-shifted variants of the green fluorescent protein. Because N-terminal palmitoylation of PSD-95 is a prerequisite for proper subcellular targeting and cluster formation,[6,19–21] CFP was fused to the C-terminal of PSD-95 (PSD-95–CFP). In turn, YFP was fused to the N-terminal of Kir2.1 in order to preserve the PDZ interaction site at the C-terminal (YFP–Kir2.1). The expression pattern of these fusion proteins did not vary from that of the native proteins as determined by immunocytochemistry. Cluster formation was independent of the expression system we used [OK, Chinese hamster ovary cells (CHO), Hek293 cells; see Fig. 1(A) and Fig. 4(A)].

The setup used for the lifetime measurements is depicted in Fig. 2. In all experiments, a mode-locked titanium:sapphire (Ti:Sa) laser (Mira 900, Coherent GmbH, Dieburg, Germany) was used for excitation of the CFP chromphore. The emission

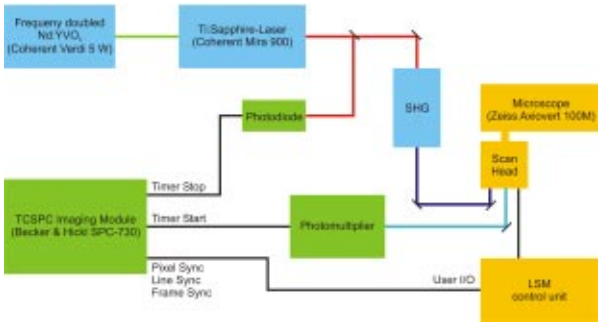

Fig. 2 Experimental setup. Femtosecond laser pulses were generated with a Ti:Sa laser that was pumped by a 5-W frequency-doubled neodymium-doped yttrium vanadate (Nd:YVO_4) laser. The frequency of the laser beam was doubled in a crystal (SHG unit). The focused beam was directed to the scan head of the laser-scanning microscope. Fluorescence light originating from the sample was guided through an optical glass fiber to a MCP-PMT for time-correlated single-photon counting. A bandpass filter in front of the MCP-PMT restricted the recorded fluorescence to the wavelength range of 465 to 495 nm. The MCP-PMT was connected to a TCSPC computer module (SPC730, Becker & Hickl), which was used to build up a three-dimensional histogram of photon density over spatial (*x,y*) and temporal (*t*) coordinates. The actual position of the scanning beam was calculated from the FrameSync, LineSync, and PixelClock signals of the laser scanning microscope. The time measurement unit of the TCSPC imaging module is operated in the "reversed start-stop" configuration. For each photon, it determines the detection time (*t*) with respect to the next laser pulse. The temporal resolution of this setup was better than 30 ps.

wavelength was tuned to 860 nm and frequency doubled to 430 nm by a β-barium borate (BBO) crystal. At this excitation wavelength, almost no YFP fluorescence was excited. In order to minimize photobleaching and photoconversion of CFP, the average excitation power was adjusted to less than 25 μW. Consistent results were achieved only under these conditions. The attenuated laser beam was directed to the scan head of the laser scanning microscope (Zeiss LSM 510, Carl Zeiss GmbH, Göttingen, Germany). Fluorescence light originating from the sample was focused on one of the pinholes of the laser scanning microscope, coupled into an optical glass fiber and guided to a multichannel plate photomultiplier tube (MCP-PMT) (3809U, Hamamatsu Photonics Deutschland GmbH, Herrsching, Germany) for time-correlated single-photon counting. A bandpass filter (XF3075 Omega optical) in front of the photomultiplier restricted the fluorescence light to be analyzed to a wavelength range of 465 to 495 nm and filtered out scattered excitation light and YFP fluorescence effectively. The MCP-PMT was connected to a TCSPC computer module (SPC730, Becker & Hickl GmbH, Berlin, Germany), which was used to build up a three-dimensional histogram of photon density over spatial (*x,y*) and temporal (*t*) coordinates. The actual position of the scanning beam was calculated from the FrameSync, LineSync, and PixelSync signals of the laser scanning microscope. The temporal resolution of this setup was better than 30 ps (FWHM). TCSPC data were analyzed with a commercial software package (SPCImage V2.4, Becker & Hickl) that uses the iterative reconvolution method to recover the fluorescence lifetime from fluorescence decay profiles obtained for each pixel. A modified Levenberg-Marquardt algorithm was used to approximate the

best parameters of a given decay. The quality of a fit was judged by the value of a reduced χ^2. A model was rejected when χ^2 exceeded a value of 1.5. In case of a multiexponential decay, average lifetimes were calculated from the parameters of the fitting procedure, the lifetime components τ_i and the amplitudes A_i according to:[22]

$$\tau_m = \Sigma A_i \tau_i / \Sigma A_i .$$

3.3 *RET between CFP and YFP Fluorophores*

Assuming that donor and acceptor molecules are separated by a fixed distance (r), the rate of energy transfer (k_T) is given by the following equations:

$$k_T = (1/\tau_D) \times (R_0/r)^6, \quad (1)$$

where τ_D is the lifetime of the donor in the absence of an acceptor.[23] R_0 is the Förster distance, at which the energy transfer efficiency (E) is 50%. The efficiency of energy transfer is defined as the fraction of photons absorbed by the donor that are transferred to the acceptor. It is given by the ratio of the transfer rate to the total decay rate of the donor:

$$E = k_T/(1/\tau_D + k_T). \quad (2)$$

The rate of energy transfer (k_T) can be determined experimentally by comparing the lifetime of the donor in the presence of an acceptor (τ_{DA}) with that of the donor in the absence of an acceptor (τ_D)

$$k_T = (1/\tau_{DA}) - (1/\tau_D). \quad (3)$$

Equations (2) and (3) can be rearranged to yield

$$E = 1 - (\tau_{DA}/\tau_D). \quad (4)$$

Thus in order to determine RET efficiency by lifetime measurements, it is only necessary to measure τ_{DA} and τ_D. Since lifetime measurements are independent of fluorescence intensity and the actual number of fluorophores present, RET and control measurements can be carried out in different cells. This is one important advantage of lifetime-based RET measurements.

Figure 3 shows representative examples of control measurements in which we determined the fluorescence lifetime of CFP in cells expressing either CFP alone [Fig. 3(A)] and PSD-95–CFP [Fig. 3(B)], or a hybrid protein, in which CFP and YFP are closely linked by a short peptide [Fig. 3(C)]. In cells expressing CFP or PSD-95–CFP, the fluorescence decay could be approximated by a monoexponential function, yielding a fluorescence lifetime of $\tau = 2.45 \pm 0.05$ ns (mean $\pm$ S.D., $n = 19$), and $\tau = 2.55 \pm 0.13$ ns ($n = 30$), respectively. Thus fusion of PSD-95 did not significantly change the fluorescence lifetime of CFP. There was only negligible variation of the fluorescence lifetime within a cell, as illustrated in the color coded fluorescence lifetime image [panel c in Fig. 3(A)–3(C)] and the lifetime distribution plot [panel e in Fig. 3(A)–(C)].

In order to assess RET efficiency between closely neighboring CFP and YFP, we constructed a YFP–CFP hybrid protein in which both fluorophores were linked by a short sequence of 18 amino acids. Xu et al. demonstrated for an analogous protein, consisting of GFP and its blue variant

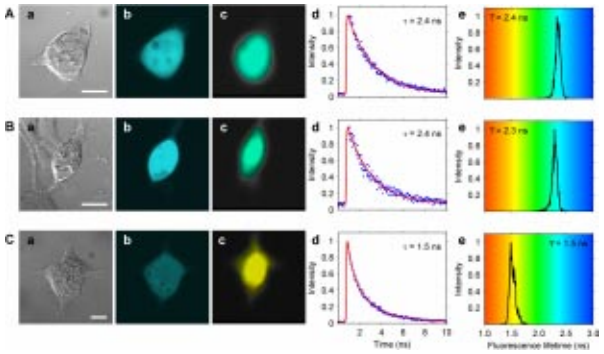

Fig. 3 Fluorescence lifetime imaging of cells expressing CFP and CFP fusion constructs. (A) Hek293 cell expressing CFP cytosolically. (a) Transmission image. Scale bar: 10 μm. (b) Fluorescence image recorded in the CFP channel. (c) Fluorescence lifetime image. Average fluorescence lifetimes are encoded by color as specified in (e) (JBO online version only). In this case, the variation of the fluorescence lifetime within the cell is small. (d) Representative fluorescence decay recorded in one pixel located in the center of the cell. The fluorescence decay could be approximated by a monoexponential function. (e) Subcellular distribution of fluorescence lifetimes. (B) Hek293 cell expressing PSD-95–CFP. As for cytosolically expressed CFP, the fluorescence lifetime image does not show any heterogeneities. The mean fluorescence lifetime is indistinguishable from that of CFP. Scale bar: 10 μm. (C) Hek293 cell expressing a YFP–CFP hybrid protein, in which CFP and YFP are closely linked by a short peptide. The fluorescence lifetime of CFP decreased considerably owing to RET between the CFP and YFP moiety. Scale bar: 10 μm.

(BFP), that RET occurs between both subunits.[24] As shown in Fig. 3(C), the fluorescence lifetime of CFP decreased significantly in cells expressing the YFP–CFP hybrid construct. The average donor lifetime was $\tau = 1.63 \pm 0.07$ ns ($n = 13$), indicating RET between the two fluorophores.

3.4 *RET between PSD-95-CFP and YFP-Kir2.1*

Figure 4(A) shows confocal micrographs of an Hek293 cell coexpressing PSD-95–CFP and YFP–Kir2.1. As resolved by the intensity profile along a representative cross-section through the cell, the two fluorescence patterns of CFP and YFP are colocalized in clustered regions, but not in the cytoplasm Fig. 4(A)d. In order to show that PSD-95–CFP and YFP–Kir2.1 not only colocalize but also interact in clustered regions, we tested whether RET occurs between their CFP and YFP fluorescence tags.

When PSD-95–CFP was coexpressed with YFP–Kir2.1, the decay kinetics of CFP fluorescence could not be approximated in all regions of the cell by a monoexponential function. In these cases, only a biexponential fit yielded satisfying χ^2 values. The lifetime image of the cell shown in Fig. 4(A) exhibits an inhomogeneous distribution of fluorescence decay constants [Fig. 4(B) a]. Clustered regions displayed short average fluorescent lifetimes of CFP (red color), whereas longer lifetimes were found in the cytoplasm (blue color).

These data demonstrate that PSD-95–CFP fluorescence was quenched by RET predominantly in clusters of PSD-95–CFP and YFP–Kir2.1, which thus resemble the sites of their physical interaction. Outside the clusters, PSD-95–CFP was far less quenched, indicating that only a few PSD-95–CFP molecules interacted with YFP–Kir2.1. Consequently, the distribution of the mean CFP fluorescence lifetimes over the en-

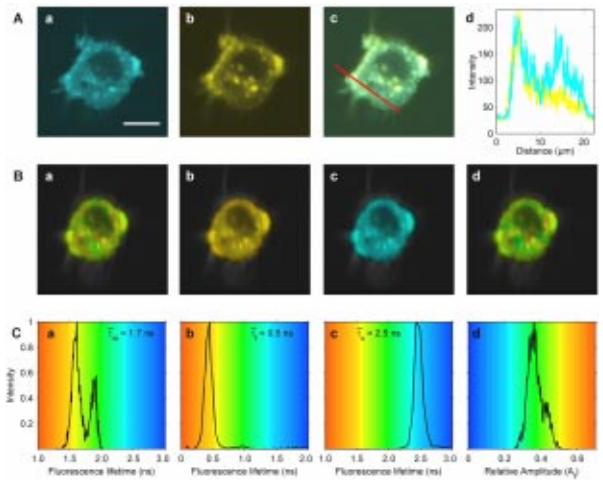

Fig. 4 RET between PSD-95–CFP and YFP–Kir2.1. (A) Confocal images of an Hek293 cell coexpressing PSD-95–CFP and YFP–Kir2.1. (a) Fluorescence image recorded in the CFP channel. Scale bar: 10 μm. (b) Fluorescence image recorded in the YFP channel. (c) Overlay of (a) and (b). (d) Fluorescence intensity profile along the red line shown in (c). PSD-95–CFP and YFP–Kir2.1 are colocalized in clustered regions, but not in the cytoplasm. (B) Fluorescence lifetime images. Fluorescence lifetimes are encoded by color as specified in the respective panels of (C) (JBO online version only). (a) Fluorescence lifetime image of the average fluorescence lifetime. Fluorescence lifetimes are shortest in clusters of PSD-95–CFP and YFP–Kir2.1. (b) Fluorescence lifetime image of the fast lifetime component (τ_f). τ_f is constant throughout the cell. It can be regarded as a property of interacting PSD-95–CFP and YFP–Kir2.1 clusters. (c) Fluorescence lifetime image and distribution of the slow lifetime component (τ_s). Also τ_s is constant throughout the cell. It can be regarded as a property of unbound PSD-95–CFP molecules. (d) Distribution of the relative amplitude (A_f) of the fast lifetime component. A_f is highest in clusters, indicating a high fraction of interacting PSD-95–CFP molecules. In contrast to this, A_f is low in cytosolic regions, indicating a high fraction of unbound PSD-95–CFP molecules. (C) Distribution of average fluorescence lifetimes (a), individual fluorescence lifetime components (b) and (c) and the relative amplitude of the fast lifetime component (d) throughout the cell.

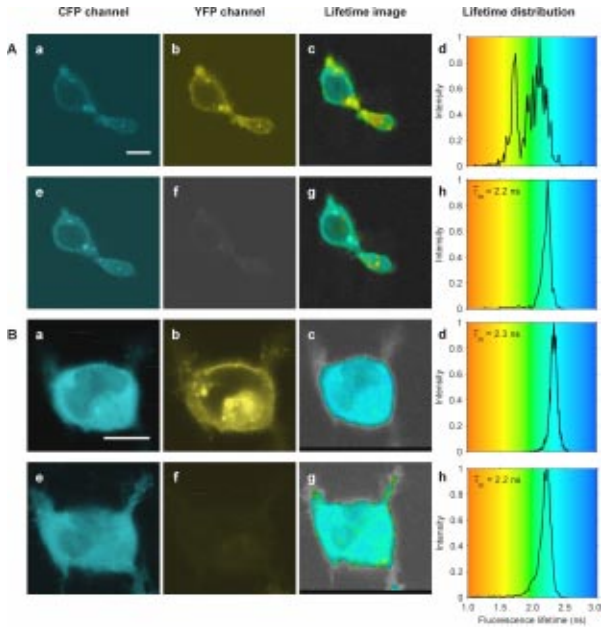

Fig. 5 CFP fluorescence lifetime recovers to control values after photodestruction of the acceptor fluorophore. (A) Confocal and fluorescence lifetime images of an Hek293 cell coexpressing PSD-95–CFP and YFP–Kir2.1 (a)–(d) before and (e)–(h) after photobleaching of the YFP moiety with the Ar 514-nm line. (f) After photobleaching, virtually no fluorescence is visible in the YFP channel. (g) and (h) CFP lifetimes rose back almost to control values. Scale bar: 10 μm. (B) Confocal and fluorescence lifetime images of an Hek293 cell coexpressing PSD-95–CFP and channel mutant YFP–Kir2.1–ΔSEI lacking the PDZ ligand motif (a)–(d) before and (e)–(h) after photobleaching. The donor decay could be approximated again by a monoexponential function. The average fluorescence lifetime [(c) and (d)] does not differ significantly from fluorescence lifetimes found in cells expressing CFP or PSD-95–CFP. (f) After photobleaching, virtually no fluorescence is visible in the YFP channel. (g) and (h) CFP lifetimes are slightly accelerated, suggesting that irradiation with the Ar 514-nm line has led to the formation of CFP photoisomers with a shorter lifetime. Scale bar: 10 μm.

tire cell exhibited two peaks [Fig. 4(C) a]. A detailed analysis of the clustered regions yielded an average CFP fluorescence lifetime of $\tau_m = 1.70 \pm 0.20$ ns ($n = 57$ clusters in 16 cells). This value is significantly shorter than the average lifetime observed in cells expressing PSD-95–CFP only and is in the same range as the average lifetime determined in cells expressing the YFP–CFP hybrid construct.

The fast and the slow fluorescence lifetime components determined by the biexponential fit were $\tau_f = 0.88 \pm 0.24$ ns and $\tau_s = 2.51 \pm 0.20$ ns, respectively. The slow lifetime component was close to the lifetimes measured for CFP and PSD-95–CFP. It can thus be attributed to unquenched, noninteracting PSD-95–CFP molecules, which are not subject to RET. In contrast to this, interacting PSD-95–CFP molecules, which were effectively quenched by RET, gave rise to the additional fast lifetime component (τ_f). Thus the respective lifetimes can be regarded as a characteristic property of bound and unbound molecules. Whereas their absolute values are constant throughout the cells [Fig. 4(B) b,c], their relative amplitudes A_f and A_s provide a rough estimate for the fraction of interacting versus noninteracting molecules. Throughout the whole cell A_f varied from 20 to 60% [Fig. 4(C) d]. Figure 4(B) d shows the subcellular distribution of the relative amplitude of τ_f (A_f). As expected, A_f was greatest (red color) in clustered regions, indicating a large fraction (up to 60%) of interacting PSD-95 molecules. A_f was smallest (blue color) in cytosolic regions (20%), indicating a large fraction of unbound molecules.

In order to verify that indeed RET and not any other quenching process caused the decrease in CFP fluorescence lifetimes in clustered regions, we bleached the acceptor fluorophore with the Ar 514-nm line. As expected, CFP lifetimes rose back to control values [Fig. 5(A) g–h]. For a negative control, we coexpressed PSD-95–CFP with the channel mutant YFP–Kir2.1–ΔSEI lacking the PDZ ligand motif [Fig. 5(b)]. In these cells, the donor decay could be approximated by a monoexponential function. The calculated mean fluorescence lifetime constant was $\tau = 2.44 \pm 0.15$ ns ($n = 32$), which does not differ significantly from fluorescence lifetimes observed in cells expressing CFP or PSD-95–CFP. A summary of the average fluorescence lifetimes of CFP in the respective experimental groups is shown in Fig. 6.

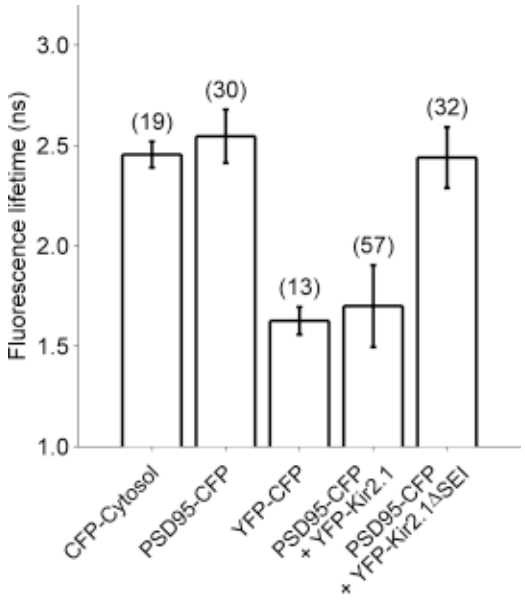

Fig. 6 Statistics of measured fluorescence lifetimes. Bar graph of the average fluorescence lifetime (τ_m) of CFP in the absence and in the presence of acceptor molecules. Lifetimes are given as mean ±S.D. The number of measurements is indicated in parentheses. The fluorescence decay of CFP or PSD-95–CFP decay could be approximated by a monoexponential function, yielding a fluorescence lifetime of $\tau = 2.45 \pm 0.05$ ns and $\tau = 2.55 \pm 0.13$ ns, respectively. Thus, fusion of PSD-95 did not significantly change the fluorescence lifetime of CFP. In the YFP–CFP hybrid protein, in which both fluorophores are linked by a short sequence of 18 amino acids, the fluorescence lifetime of CFP decreased significantly ($\tau_m = 1.63 \pm 0.07$ ns) owing to RET. Average fluorescence lifetimes in clusters of PSD-95–CFP and YFP–Kir2.1 are in the same range ($\tau_m = 1.70 \pm 0.20$ ns). The fast and the slow fluorescence lifetime components determined by the biexponential fit were $\tau_f = 0.88 \pm 0.24$ ns and $\tau_s = 2.51 \pm 0.20$ ns, respectively. Thus, owing to the interaction between PSD and Kir2.1, both fluorescence tags are brought into close vicinity, giving rise to RET. RET could not be observed upon coexpression of PSD-95–CFP with the channel mutant YFP–Kir2.1–ΔSEI lacking the PDZ ligand motif. In these cells, the donor decay could be approximated by a monoexponential function, yielding a mean fluorescence lifetime constant of $\tau = 2.44 \pm 0.15$ ns, which did not differ significantly from fluorescence lifetimes observed in cells expressing CFP or PSD-95–CFP.

4 Conclusions and Perspectives

This study demonstrates how time domain-based fluorescence lifetime imaging techniques can be used to visualize and quantify the extent of RET between interacting proteins in living cells. The technique takes advantage of the high temporal resolution of an MCP-PMT and the high spatial resolution of a confocal laser scanning microscope. The use of fluorescent proteins as donor and acceptor moieties allows us to apply this technique in living cells.

Here we employed this technique to describe the PDZ-mediated interaction between a neuronal MAGUK protein and a potassium channel. Heterologous coexpression of PSD-95 clusters the potassium inward rectifier channel Kir2.1. Our fluorescence lifetime measurements show that within these clusters both proteins not only colocalize but also interact with each other. We conclude this from the significant decrease in donor fluorescence lifetime, with values in the range found for CFP covalently linked to YFP. This decrease in fluorescence lifetime was mediated by RET and not any other quenching process, because it could be reversed by photodestruction of the acceptor fluorophore. There was no change in donor fluorescence lifetime upon coexpression of PSD-95–CFP and the noninteracting channel mutant YFP–Kir2.1–ΔSEI, indicating that only a specific interaction, not an accidental colocalization, is sufficient for RET to occur. Since donor fluorescence decayed biexponentially in cells coexpressing PSD-95–CFP and YFP–Kir2.1, our RET results allowed us to distinguish between two subpopulations of PSD-95–CFP molecules: an interacting population that is quenched by RET, giving rise to a fast component in the CFP fluorescence decay and a noninteracting fraction that is unaffected by RET, producing the same fluorescence lifetime as CFP expressed alone.

Whereas the absolute value of the fast decay component provides information about the spatial proximity between the fluorophores involved in RET, its relative amplitude roughly estimates the amount of interacting molecules. From the fast component of the donor fluorescence lifetime of 0.88 ns, a RET efficiency of 67% can be calculated. This would correspond to a distance of 4.5 nm between donor and acceptor moieties, assuming a Förster radius of 4.9 nm for CFP and YFP and random orientation between the two fluorophores.[25] Thus clustering of YFP–Kir2.1 by PSD-95–CFP must bring the two fluorophores into close proximity.

So far, the molecular mechanisms and the stoichiometry by which PSD-95 clusters potassium channels are not known. Initial hypotheses relying on the multivalent properties of PSD-95 and the channel subunits have been questioned. Recent data show that the ability of PSD-95 to cluster Kv1.4 channels does not depend on its ability to form multimers at all, but only requires N-terminal palmitoylation and a tetrameric channel structure.[26] In light of these results, our data are in good agreement with the hypothesis that an intramolecular interaction of the SH3 and GK domains of PSD-95 backfolds the PSD-95 molecule, thereby approximating its own C-terminus and the N-terminus of the PDZ-interacting channel subunit.[27–28]

Since the present technique allows quantification of protein–protein interactions with both high spatial and high temporal resolution, future application will focus on interaction dynamics. Of particular interest would be a detailed analysis of regulated PDZ interactions, which have been implicated in synaptic development or plasticity.[29,30]

Acknowledgments

The study was supported by the Deutsche Forschungsgemeinschaft SFB430-A2 to N.K. We are grateful to Karin Schoknecht and Andrea Kolchmeier for excellent technical assistance.

References

1. S. K. Kim, ''Polarized signaling: basolateral receptor localization in epithelial cells by PDZ-containing proteins,'' *Curr. Opin. Cell Biol.* **9**, 853–859 (1997).
2. S. E. Craven and D. S. Bredt, ''PDZ proteins organize synaptic signaling pathways,'' *Cell* **93**, 495–498 (1998).
3. C. C. Garner, J. Nash, and R. L. Huganir, ''PDZ domains in synapse assembly and signaling,'' *Trends Cell Biol.* **10**, 274–280 (2000).
4. M. Sheng and C. Sala, ''PDZ domains and the organization of supramolecular complexes,'' *Annu. Rev. Neurosci.* **24**, 1–29 (2001).

5. M. Migaud, P. Charlesworth, M. Dempster, L. C. Webster, A. M. Watabe, M. Makhinson, Y. He, M. F. Ramsay, R. G. Morris, J. H. Morrison, T. J. O'Dell, and S. G. Grant, ''Enhanced long-term potentiation and impaired learning in mice with mutant postsynaptic density-95 protein,'' *Nature (London)* **396**, 433–439 (1998).
6. A. E. El-Husseini, E. Schnell, D. M. Chetkovich, R. A. Nicoll, and D. S. Bredt, ''PSD-95 involvement in maturation of excitatory synapses,'' *Science* **290**, 1364–1368 (2000).
7. S. Tomita, R. A. Nicoll, and D. S. Bredt, ''PDZ protein interactions regulating glutamate receptor function and plasticity,'' *J. Cell Biol.* **153**, F19–F24 (2001).
8. T. Förster, ''Energiewanderung und Fluoreszenz,'' *Naturwissenschaften* **6**, 166–175 (1946).
9. T. Förster, ''Experimentelle und theoretische Untersuchung des zwischenmolekularen Überganges von Elektronenanregungsenergie,'' *Z. Naturforsch. A* **4A**, 321–327 (1949).
10. T. Förster, ''Transfer mechanisms of electronic excitation,'' *Discuss. Faraday Soc.* **27**, 7–17 (1959).
11. S. Latt, H. T. Cheung, and E. R. Blout, ''Energy transfer: a system with relatively fixed donor-acceptor separation,'' *J. Am. Chem. Soc.* **87**, 995–1003 (1965).
12. L. Stryer and R. P. Haugland, ''Energy transfer: a spectroscopic ruler,'' *Proc. Natl. Acad. Sci. U.S.A.* **58**, 719–726 (1967).
13. L. Trón, J. Szöllösi, S. Damjanovich, S. H. Helliwell, D. J. Arndt-Jovin, and T. M. Jovin, ''Flow cytometric measurement of fluorescence resonance energy transfer on cell surfaces. Quantitative evaluation of the transfer efficiency on a cell-by-cell basis,'' *Biophys. J.* **45**, 939–946 (1984).
14. G. W. Gordon, G. Berry, X. H. Liang, B. Levine, and B. Herman, ''Quantitative fluorescence resonance energy transfer measurements using fluorescence microscopy,'' *Biophys. J.* **74**, 2702–2713 (1998).
15. C. Stockklausner, J. Ludwig, J. P. Ruppersberg, and N. Klöcker, ''A sequence motif responsible for ER export and surface expression of Kir2.0 inward rectifier K^+ channels,'' *FEBS Lett.* **247**, 1–5 (2001).
16. B. Z. Harris and W. A. Lim, ''Mechanism and role of PDZ domains in signaling complex assembly,'' *J. Cell. Sci.* **114**, 3219–3231 (2001).
17. J. F. Long, H. Tochio, P. Wang, J. S. Fan, C. Sala, M. Niethammer, M. Sheng, and M. Zhang, ''Supramodular structure and synergistic target binding of the N-terminal tandem PDZ domains of PSD-95,'' *J. Mol. Biol.* **327**, 203–214 (2003).
18. R. B. Nehring, E. Wischmeyer, F. Doring, R. W. Veh, M. Sheng, and A. Karschin, ''Neuronal inwardly rectifying K^+ channels differentially couple to PDZ proteins of the PSD-95/SAP90 family,'' *J. Neurosci.* **20**, 156–162 (2000).
19. Y. P. Hsueh and M. Sheng, ''Requirement of N-terminal cysteines of PSD-95 for PSD-95 multimerization and ternary complex formation, but not for binding to potassium channel $K_v1.4$,'' *J. Biol. Chem.* **274**, 532–536 (1999).
20. J. R. Topinka and D. S. Bredt, ''N-terminal palmitoylation of PSD-95 regulates association with cell membranes and interaction with K^+ channel $K_v1.4$,'' *Neuron* **20**, 125–134 (1998).
21. S. E. Craven, A. E. El-Husseini, and D. S. Bredt, ''Synaptic targeting of the postsynaptic density protein PSD-95 mediated by lipid and protein motifs,'' *Neuron* **22**, 497–509 (1999).
22. J. R. Lakowicz, *Principles of Fluorescence Spectroscopy*, Kluwer Academic/Plenum, New York (1999).
23. R. M. Clegg, ''Fluorescence resonance energy transfer,'' in *Fluorescence Imaging Spectroscopy and Microscopy*, X. F. Wang and B. Herman, Eds., pp. 179–252, Wiley, New York (1996).
24. X. Xu, A. L. V. Gerard, B. C. B. Huang, D. C. Anderson, D. G. Payan, and Y. Luo, ''Detection of programmed cell death using fluorescence energy transfer,'' *Nucleic Acids Res.* **26**, 2034–2035 (1998).
25. G. H. Patterson, D. W. Piston, and B. G. Barisas, ''Förster distances between green fluorescent protein pairs,'' *Anal. Biochem.* **284**, 438–440 (2000).
26. K. S. Christopherson, N. T. Sweeney, S. E. Craven, R. Kang, A. E. El-Husseini, and D. S. Bredt, ''Lipid and protein mediated multimerization of PSD-95: implications for receptor clustering and assembly of synaptic protein networks,'' *J. Cell. Sci.* **116**, 3213–3219 (2003).
27. A. W. McGee and D. S. Bredt, ''Identification of an intramolecular interaction between the SH3 and guanylate kinase domains of PSD-95,'' *J. Biol. Chem.* **274**, 17431–17436 (1999).
28. A. W. McGee, S. R. Dakoji, O. Olsen, D. S. Bredt, W. A. Lim, and K. E. Prehoda, ''Structure of the SH3-guanylate kinase module from PSD-95 suggests a mechanism for regulated assembly of MAGUK scaffolding proteins,'' *Mol. Cell* **8**, 1291–1301 (2001).
29. D. M. Chetkovich, L. Chen, T. J. Stocker, R. A. Nicoll, and D. S. Bredt, ''Phosphorylation of the postsynaptic density-95 (PSD-95)/discs large/zona occludens-1 binding site of stargazin regulates binding to PSD-95 and synaptic targeting of AMPA receptors,'' *J. Neurosci.* **22**, 5791–5796 (2002).
30. J. Choi, J. Ko, E. Park, J. R. Lee, J. Yoon, S. Lim, and E. Kim, ''Phosphorylation of stargazin by protein kinase A regulates its interaction with PSD-95,'' *J. Biol. Chem.* **277**, 12359–12363 (2002).